Check for updates

ADVANCED OPTICAL MATERIALS
www.advopticalmat.de

Remarkable Isomer Effect on the Performance of Fully Non-Fused Non-Fullerene Acceptors in Near-Infrared Organic Photodetectors

Xiantao Hu, Zhuoran Qiao, Davide Nodari, Qiao He, Jesika Asatryan, Martina Rimmele, Zhili Chen, Jaime Martín, Nicola Gasparini, and Martin Heeney**

Two fully non-fused small-molecule acceptors BTIC-1 and BTIC-2 are reported for application in near-infrared organic photodetectors (NIR OPDs). Both acceptors contain the same conjugated backbone but differing sidechain regiochemistry, affording significant differences in their optical properties. The head-to-head arrangement of BTIC-2 results in a reduction of optical band gap of 0.17 eV compared to BTIC-1, which contains a head-to-tail arrangement, with absorption spanning the visible and near-IR regions up to 900 nm. These differences are rationalized on the basis of non-covalent intramolecular interactions facilitating a more co-planar conformation for BTIC-2. OPDs based on PM6:BTIC-2 deliver a low dark current density of 2.4×10^{-7} A cm^{-2}, leading to a superior specific detectivity of 1.7 × 1011 Jones at 828 nm at -2 V. The optimized device exhibits an ultrafast photo response of 2.6 µs and a high -3 dB cut-off frequency of 130 kHz. This work demonstrates that fully non-fused small-molecule acceptors offer competitive device performance for NIR OPDs compared to fused-ring electron acceptors, but with reduced synthetic complexity. Furthermore, the study presents an efficient strategy to enhance device performance by varying conformational locks.

1. Introduction

Photodetectors (PDs) convert incoming optical signals into electrical signals and are widely used in applications such as biomedical imaging, environmental monitoring, optical communication, machine vision, etc.[1–4] The current commercial photodetector market is dominated by devices based on inorganic semiconductors like silicon (Si) and indium gallium arsenide (InGaAs) due to their excellent charge-carrier mobility, small exciton binding energy and high stability.[5,6] Applying optoelectronic functions onto flexible and soft surfaces, especially human skin, is at the forefront of multidisciplinary research. In particular, with the rapid development of wearable electronics, the demand for highly flexible and stretchable PDs, which can be adhered onto curved surfaces or interfaced with the human body, is continuously increasing.[6,7] However, the intrinsic features of inorganic semiconductors, such as the high brittleness and the complicated manufacturing process, make it expensive or very complex to meet this demand.[1,8] To circumvent these limitations, great effort has been put into developing novel solution-processable semiconductor materials, including colloidal quantum dots (QDs),[7,9,10] perovskites[11,12] and 2D materials.[13,14] These materials have demonstrated excellent mechanical flexibility, solution processability, chemical versatility and promising optoelectronic properties.[15–17] However they also have shortcomings such as the toxic materials contained in QDs and perovskites, limited spectral response and/or poor air stability.[7,18]

X. Hu, Z. Qiao, D. Nodari, Q. He, M. Rimmele, Z. Chen, N. Gasparini, M. Heeney
Department of Chemistry
Imperial College London
White City Campus, London W12 0BZ, UK
E-mail: n.gasparini@imperial.ac.uk; m.heeney@imperial.ac.uk

The ORCID identification number(s) for the author(s) of this article can be found under https://doi.org/10.1002/adom.202302210

© 2023 The Authors. Advanced Optical Materials published by Wiley-VCH GmbH. This is an open access article under the terms of the Creative Commons Attribution License, which permits use, distribution and reproduction in any medium, provided the original work is properly cited.

DOI: 10.1002/adom.202302210

X. Hu, Z. Qiao, D. Nodari, Q. He, M. Rimmele, N. Gasparini, M. Heeney
Centre for Processable Electronics
Imperial College London
South Kensington Campus, London SW7 2BZ, UK

J. Asatryan, J. Martín
Centro de Investigacións Tecnolóxicas (CIT)
Grupo de Polímeros
Universidade da Coruña
Esteiro, Ferrol 15471, Spain

M. Heeney
Division of Physical Sciences and Engineering
KAUST Solar Centre
King Abdullah University of Science and Technology
Thuwal 23955-6900, Saudi Arabia

Thus new materials and approaches are required to overcome these limitations.

In the past decades, organic photodetectors (OPDs) have attracted much interest due to their inherent advantages, including detection wavelength tunability, low weight, mechanical flexibility, and large-area processability.[3,19,20] Since the fabrication of the first OPD in 1981,[21] using small-molecule dyes merocyanine and rhodamine B, OPDs based on small molecules and polymers have entered a period of rapid development. According to the detection wavelength, OPDs can be categorized as ultraviolet (UV)-, visible-, infrared (IR)-, x-ray- and γ-ray detectors.[16] Recently, near infrared (NIR) OPDs have drawn attention owing to their potential application in optical communication, security surveillance, remote sensing, and medical imaging. The latter application is driven by the long propagation distance of NIR light with low attenuation within biological tissues.[14,18,22–24] Benefitting from the rapid development of organic photovoltaic materials, the detection wavelength of OPDs spans the UV–vis-NIR region, with the response spectrum of NIR OPDs extending to over 900 nm,[25–28] and in some cases beyond 1000 nm.[25,29–34]

Significant progress in the performance of NIR OPDs have been achieved in recent years, especial with regard to extending and flattening the response range through advanced materials and device engineering.[5,35] However, further improvement in responsivity (R) and specific detectivity (D^*) of NIR OPDs has been hindered by the poor exciton dissociation efficiency in NIR materials owing to the high non-radiative recombination at narrow band gaps.[22,36] Operating the device with an external negative bias assists exciton dissociation but in the meantime increases the dark current density (J_D) due to increased charge injection from electrode, especially when the band gap of the semiconductor material becomes smaller.[15,37,38] In addition, energetic disorder, active layer morphology and charge recombination processes have an effect on J_D.[39–41] As a result, the detection ability of NIR OPDs is limited, as R and D^* are significantly dependent on high photocurrent and low dark current densities.[22] Therefore, suppressing the dark current in NIR OPDs has become a critical issue for their commercialization, and considerable effort has been devoted to the simultaneous minimization of the dark current and the maintenance of high R and D^*.[42–44] Recently the application of non-fullerene acceptors (NFAs) has attracted increasing interest, as they can reduce the dark current with minimal loss in the R or EQE.[40,45,46] For instance, Chen and co-workers reported NIR OPDs using four ultra-narrow band gap NFAs with different side chains as acceptors, and obtained a low dark current of 8×10^{-11} A at a bias voltage of −0.1 mV and excellent detectivity of $> 2.5 \times 10^{11}$ Jones at 880 nm. The response width at -3 dB point frequency reached 11.78 kHz.[25] Würthner and co-workers demonstrated a NIR OPD based on J-type coupled squaraine dye SQ-H, which exhibited a responsivity of 0.1 A W^{-1} and 4×10^{10} Jones under illumination with 1050 nm at 0 V.[29] Zhu and co-workers constructed a highly sensitive NIR OPDs based on PM6:PDTTIC-4F and delivered a high responsivity of 0.55 A W^{-1} (900 nm) and excellent detectivity of over 10^{13} Jones by suppressing the dark current via modulation of the film thickness.[30]

It is worth noting that most of the NFAs used in OPDs possess a fused-ring ladder-type backbone to yield a rigid and planar conformation.[47] However the synthetic complexity of such species can be high, which can potentially hinder their large scale preparation and implementation.[25,38,48] On this basis, various non-fused small-molecule acceptors (NFSMAs) have been reported, exploiting non-covalent interactions between adjacent aromatics or steric hindrance from the side chains to help reinforce molecular planarity. The use of convergent synthetic approaches aides structural tuning and facilitates upscaling. NFSMAs have demonstrated excellent photovoltaic performance in organic photovoltaics (OPVs), with the leading power conversion efficiency (PCE) approaching ≈15%.[49,50] However OPDs using NFSMAs have rarely been studied, especially those with NIR absorption.[18,51] Hence, the design and OPD application of efficient partially or fully non-fused NIR NFAs is still a challenge.

Based on the above considerations, we designed two non-fused NFAs which only differ in the regiochemistry of the solubilizing groups. The molecular design builds on the established acceptor (A) -donor (D)-acceptor (A) concept, in which the band gap of the resulting molecule can be tuned to a first approximation by the choice of D and A units. We focused on fluorinated 1,1-dicyanomethylene-3-indanone as the accepting end group due to its established utility in high performance NFAs.[52–54] For the donor core, we were interested in a thiophene-phenylene-thiophene system, due to its synthetic simplicity and the availability of suitable building blocks. The utility of this core as an acceptor has been demonstrated in OPV devices exhibiting excellent stability.[55–56] In order to push the molecular absorption toward the near-IR we reasoned that mesomerically donating groups would be required on the donor core to increase its electron density. We therefore chose to include alkoxy groups on both the phenylene and the thiophene substituents. As well as their mesomeric donating effect, they also provide solubility.

Thus, we report the synthesis of two novel fully non-fused NFAs, named BTIC-1, and BTIC-2, with the same conjugated backbone but with differing sidechain regiochemistry. This is shown to result in remarkable differences in their optical properties, with a reduction in band gap of 0.17 eV for BTIC-2 containing a head-to-head alkoxy linkage, compared to BTIC-1 with a head-to-tail arrangement. Theoretical calculations revealed that BTIC-2 has a more planar backbone conformation than BTIC-1, and thus exhibited a more red-shifted absorption profile up to 900 nm. Both materials were investigated in OPDs. BTIC-2-based OPDs have a low dark current density of 2.4×10^{-7} A cm^{-2}, leading to a high specific detectivity of 1.7×10^{11} Jones at 828 nm under reverse bias of -2 V. The optimized OPD exhibits ultrafast average rise and fall times of 2.6 and 3.3 μs respectively, and a high f_{-3dB} of 130 kHz, showing great potential for practical application in light-sensing devices. Moreover, the molecular stacking behavior and morphology were studied, which indicated that the conformation of the molecular structure together with film morphologies are critical for the OPD device performance. To the best of our knowledge, this work demonstrates the first OPDs using fully non-fused NFAs.

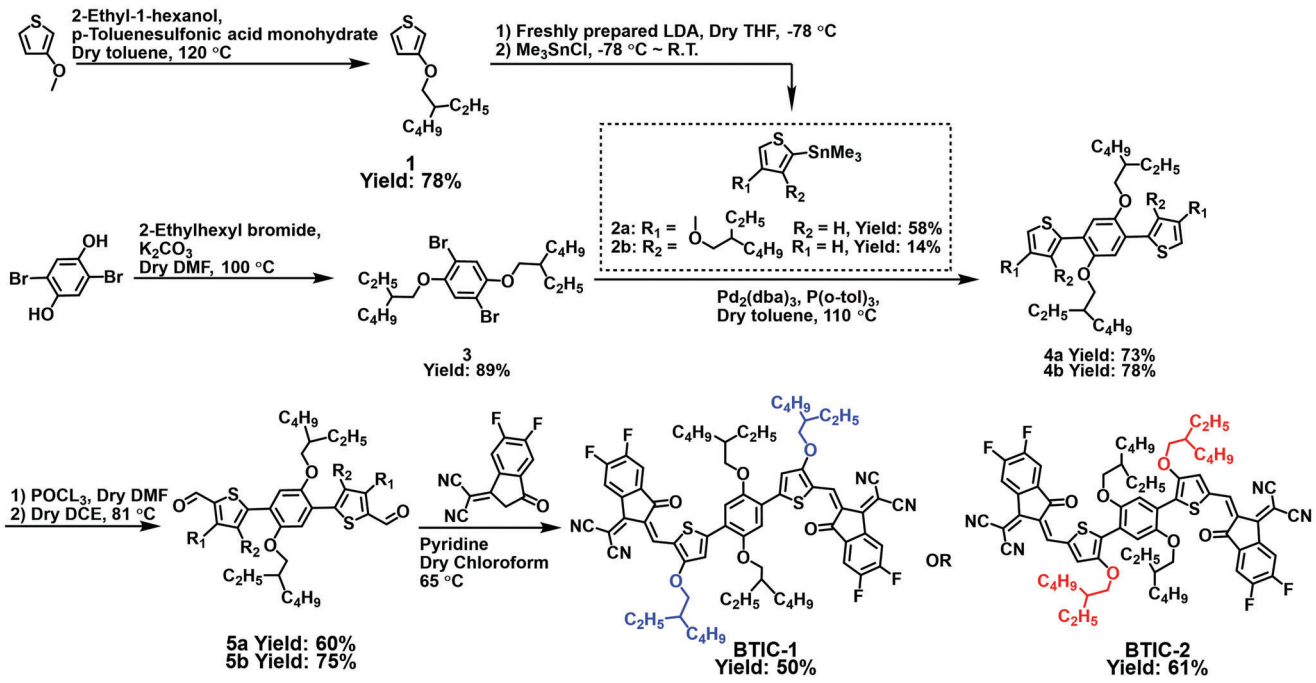
2. Results and Discussion

2.1. Synthesis and Characterization

The synthetic route to BTIC-1 and BTIC-2 is illustrated in Scheme 1, and all the detailed experimental procedures are

© 2023 The Authors. Advanced Optical Materials published by Wiley-VCH GmbH

21951071, 2024, 6, Downloaded from https://onlinelibrary.wiley.com/doi/10.1002/adom.202302210 by Test, Wiley Online Library on [08/04/2024]. See the Terms and Conditions (https://onlinelibrary.wiley.com/terms-and-conditions) on Wiley Online Library for rules of use; OA articles are governed by the applicable Creative Commons License



Scheme 1. Synthetic route towards **BTIC-1** and **BTIC-2**.

reported in the supporting information (SI). Starting from 3-methoxythiophene, a branched 2-ethylhexyl sidechain was introduced by *p*-toluenesulfonic acid catalysed transetherification with 2-ethyl-hexanol to afford **1**. Treatment of compound **1** with freshly prepared LDA followed by reaction with trimethyltin chloride gave a mixture of isomers **2a** and **2b** (m/m = 4:1), as observed by ^{1}H NMR of the crude product. Attempts to separate the isomers were complicated by the instability of stannyl compounds to silica gel and alumina, and the fact that the product was an oil rather than a crystalline compound. Therefore, purification was performed by preparative recycling GPC with chloroform as the eluent. Due to the similar molecular shape, separation required many column passes but eventually afforded **2a** and **2b** in yields of 58% and 14% respectively. The isomers were identified on the basis of chemical shift and coupling constant differences in their ^{1}H NMR spectra, with the more shielded proton in the 2-position clearly visible in **2a** (Figure S3, Supporting Information). 3-Alkylated thiophenes can be selectively deprotonated in the 5-position with bulky bases like LDA,[57] and we ascribe the reduced selectivity in the current cases to the smaller size of the alkoxy group in comparison to a methylene, coupled with the directing group effect of oxygen lone pair.

Compound **3** was synthesized following previous literature procedures.[58] Subsequent Stille coupling with compound **2a-b** using $Pd_2(dba)_3$ catalyst and P(*o*-tolyl)$_3$ ligand proceeded smoothly and the resulting products were formylated under Vilsmeier-Haack conditions using phosphorus oxychloride ($POCl_3$) in DMF to afford compound **5a-b**. Finally, Knoevenagel condensation between compound **5a-b** and the electron-withdrawing unit IC-4F yielded the target molecules BTIC-1 and BTIC-2 after chromatographic purification as intensely colored solids. Both materials exhibited good solubility in common organic solvent including chloroform and chlorobenzene at room temperature. The chemical structures of all materials were fully characterized by a combination of high-resolution mass spectrometry (HRMS) or matrix-assisted laser desorption/ionization time-of-flight (MALDI-TOF), and ^{1}H, ^{13}C and ^{19}F nuclear magnetic resonance (NMR). Both materials exhibited good thermal stability by thermal gravimetric analysis (TGA) under nitrogen flow, with the 5 wt% weight loss at 325 °C (Figure S30a, Supporting Information). No clear thermal transitions were observed for either material by differential scanning calorimetry up to their thermal decomposition temperature (Figure S30b, Supporting Information). Since both materials exhibit clear signs of crystallinity (vide infra), their melt temperature must be above the onset of degradation.

2.2. Optical and Electrochemical Properties

The optical properties of BTIC-1 and BTIC-2 were examined by UV–vis absorption spectroscopy, as both thin films and solution (**Figure 1**a). BTIC-1 exhibits a strong absorption in the region from 480 to 725 nm in chloroform with a maximum extinction coefficient of 2.47×10^5 M^{-1} cm^{-1} at 650 nm. BTIC-2 in chloroform exhibits a broader absorption between 523 and 832 nm, with the maximum absorption peak red-shifted by 77 to 727 nm and a significant increase in the maximum extinction coefficient (4.95×10^5 M^{-1} cm^{-1}). Upon moving to the film state, the absorption maxima of both materials are red-shifted by ≈100 nm to 743 nm for BTIC-1 and 828 nm for BTIC-2 with respect to their absorption in the solution state, due to the enhanced planarity caused by the inter- and intramolecular interactions in films. Moreover, the BTIC-2 film shows a more extended absorption into the near IR region up to 900 nm, relative to BTIC-1 (800 nm). The optical band gaps (E_g^{opt}) is calculated to be 1.58 eV for BTIC-1 and

© 2023 The Authors. Advanced Optical Materials published by Wiley-VCH GmbH

21951071, 2024, 6, Downloaded from https://onlinelibrary.wiley.com/doi/10.1002/adom.202302210 by Test, Wiley Online Library on [08/04/2024]. See the Terms and Conditions (https://onlinelibrary.wiley.com/terms-and-conditions) on Wiley Online Library for rules of use; OA articles are governed by the applicable Creative Commons License

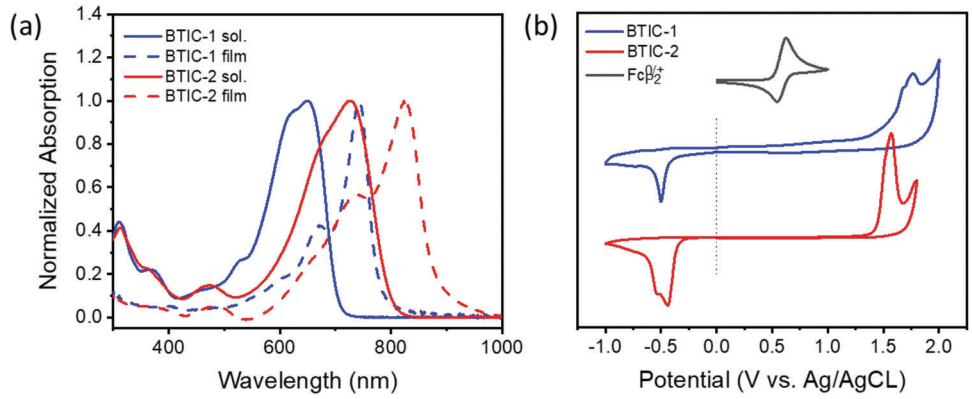


Figure 1. a) Normalized UV–vis absorption spectra of BTIC-1 and BTIC-2 in chloroform (1.26×10^{-6} M) and as thin films. b) Cyclic voltammetry curves of BTIC-1 and BTIC-2. Measurements were performed in acetonitrile/[n-Bu_4N]PF_6 solutions (0.1 M). Scan rate: 0.1 V s^{-1}.

Table 1. Summary of the optical and electrochemical properties of the BTIC-1 and BTIC-2.

	UV–vis					CV				
	λ_{max} [nm] Sol.[a)]	λ_{max} [nm] film	Molar extinction coefficient[a)] [mol L^{-1} cm^{-1}]	λ_{onset}^{film} [nm]	E_g^{opt} [eV]	E_{onset}^{ox} [V]	E_{onset}^{re} [V]	E_{HOMO} [eV]	E_{LUMO} [eV]	E_g [eV]
BTIC-1	650	743	2.47 × 105	785	1.58	1.41	−0.43	−5.63	−3.79	1.97
BTIC-2	727	828	4.95 × 105	882	1.41	1.43	−0.35	−5.65	−3.87	1.91

[a)] In chloroform.

1.41 eV for BTIC-2 from the film absorption onsets of 785 and 882 nm respectively, using the Equation (1).[59]

$$E_g^{opt} = 1240/\lambda_{onset}^{film} \text{ (eV)} \quad (1)$$

These are remarkable differences considering the two isomers only differ in the regiochemistry of the alkoxy sidechain.

The electrochemical properties of both materials were investigated by cyclic voltammetry in thin films. As shown in Figure 1b, oxidation results in non-reversible peaks, with an onset at 1.41 and 1.43 V for BTIC-1 and BTIC-2 respectively. The HOMO energy levels are estimated to be −5.63 eV for BTIC-1 and −5.65 eV for BTIC-2, using the ferrocene/ferrocenium couple (Equation (2)).[60]

$$E_{HOMO/LUMO} = -\left[4.8 + E_{onset}^{ox/re} - E_{Fc}^{0/+}\right] \text{ eV} \quad (2)$$

The LUMO energy levels of BTIC-1 and BTIC-2 are estimated to be −3.79/−3.87 eV from their reduction onsets at −0.43/−0.35 V respectively (**Table 1**). The slightly narrower electrochemical band gap of BTIC-2 agrees well with the more red-shifted absorption profile in Figure 1a.

2.3. Theoretical Calculations

To help explain the observed differences between the two isomers, the frontier molecular orbitals and molecular geometry of BTIC-1 and BTIC-2 were calculated using density functional theory (DFT) with B3LYP/6-31G (d, p) as the basis set and methyl groups instead of long alkyl chain for simplicity.[61] The predicted molecular geometries are shown in **Figure 2.** BTIC-1 is predicted to have two energy minima, shown as BTIC-1 and BTIC-1′ in Figure 2a, which differ with respect to the orientation of the alkoxy group and the adjacent thienyl group. The lowest energy conformer (BTIC-1) is shown in Figure 2b and has the alkoxy oxygen atom in close proximity to the hydrogen of the thienyl group, with a dihedral angle of 20° between the two units. A potential energy scan, in which the dihedral angle between the central benzene unit and adjacent thiophene unit was fixed, while allowing the rest of the molecule to relax to its minimum energy conformation, is shown in Figure 2c.[62] This shows the relative energy difference between the two conformers was small, <0.05 eV, and that both conformers were slightly twisted from coplanarity.

In contrast, the calculations for BTIC-2 show a strong preference for a single conformer in which the alkoxy groups on the phenyl and thiophene have a trans-like arrangement (Figure 2b). This conformation is predicted to be fully coplanar, with possible non-covalent interactions between O···S and H···O, as the intramolecular distance were calculated to be 2.63 and 2.05 Å for O···S and H···O respectively, much shorter than the sum of the van der Waals radii of O and S (3.32 Å), O and H (2.72 Å). The potential energy scan (Figure 2c) shows that the alternative arrangement, in which both alkoxy groups are cis, is significantly higher in energy and substantially twisted from coplanarity. Intuitively this makes sense, as coplanarity would force both electronegative oxygen atoms into close proximity. This relatively high energy of the cis conformer means the energetic barrier to overcome to take the lowest energy conformation is low, substantially lower than for the BTIC-1′ to interconvert to BTIC-1. Thus, we expect that

© 2023 The Authors. Advanced Optical Materials published by Wiley-VCH GmbH

21951071, 2024, 6, Downloaded from https://onlinelibrary.wiley.com/doi/10.1002/adom.202302210 by Test, Wiley Online Library on [08/04/2024]. See the Terms and Conditions (https://onlinelibrary.wiley.com/terms-and-conditions) on Wiley Online Library for rules of use; OA articles are governed by the applicable Creative Commons License

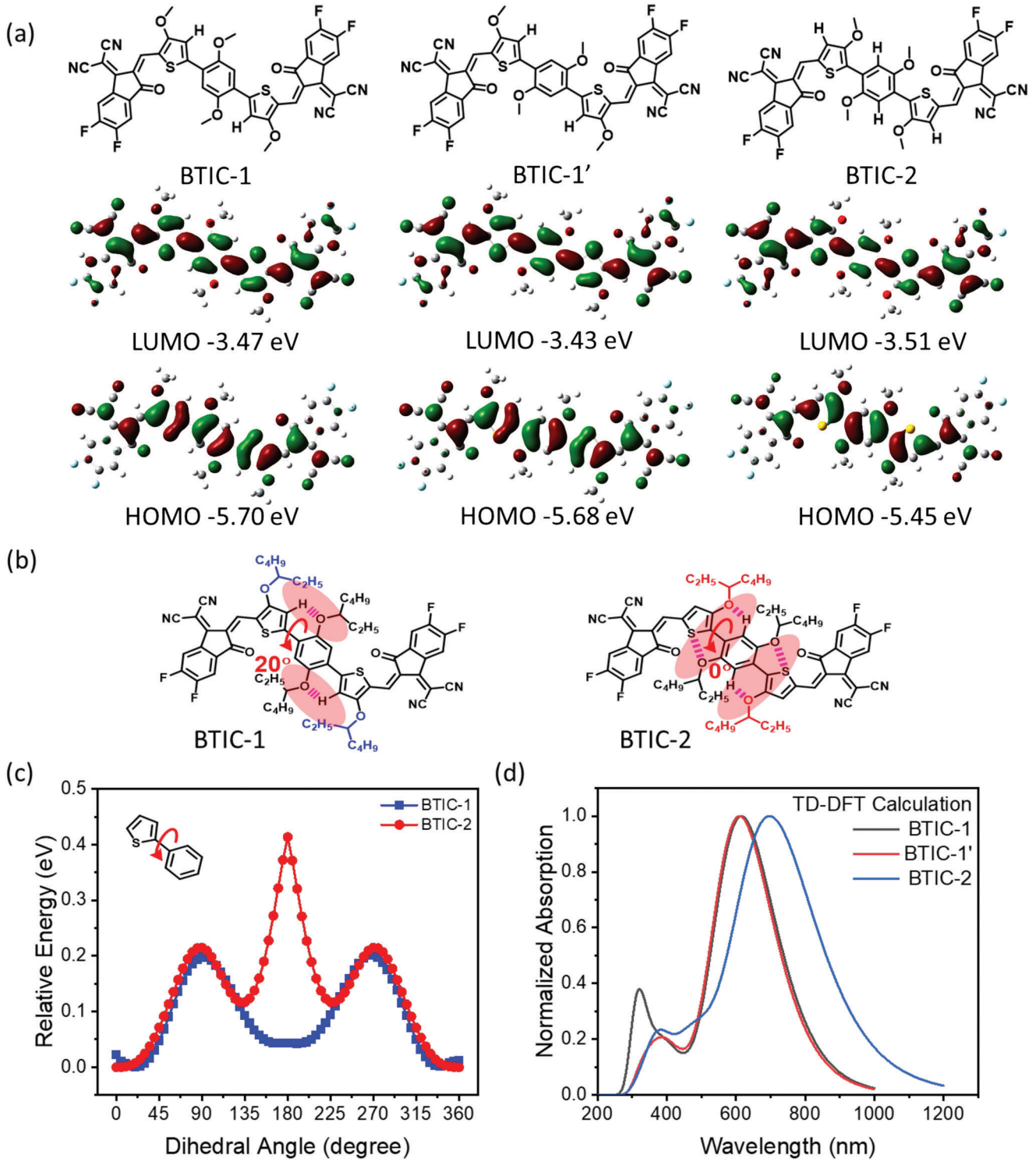


Figure 2. Theoretical calculation of BTIC-1, BTIC-1′, and BTIC-2. a) Chemical structure and frontier molecular orbitals. b) Optimized geometry at the lowest energy. c) DFT-calculated relaxed potential energy scans. d) TD-DFT-calculated UV–vis absorption spectra.

© 2023 The Authors. Advanced Optical Materials published by Wiley-VCH GmbH

21951071, 2024, 6, Downloaded from https://onlinelibrary.wiley.com/doi/10.1002/adom.202302210 by Test, Wiley Online Library on [08/04/2024]. See the Terms and Conditions (https://onlinelibrary.wiley.com/terms-and-conditions) on Wiley Online Library for rules of use; OA articles are governed by the applicable Creative Commons License

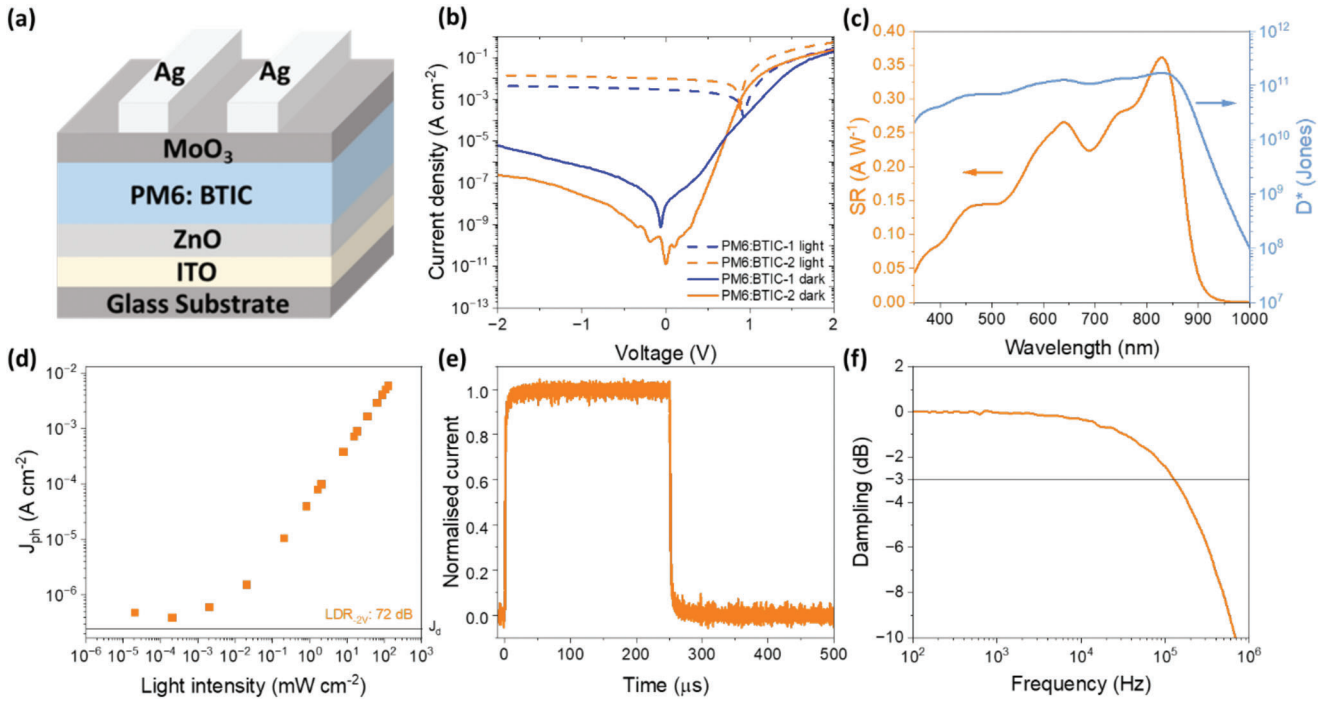


Figure 3. a) Device structure of OPDs. b) The *J–V* curves of OPDs under AM 1.5 G illumination (100 mW cm^{-2}) and in dark conditions. c) Spectral responsivity and Detectivity of PM6:BTIC-2 at -2 V. d) Linear dynamic range of PM6:BTIC-2 at -2 V under white light illumination. e) Response to temporal square-wave signals of PM6:BTIC-2 photodetector at -2 V and 2 kHz under white light illumination. f) Cut-off frequency of PM6:BTIC-2 at -2 V under white light illumination.

majority of BTIC-2 molecules adopt the trans-like planar conformation, whereas for BTIC-1 it will be more mixed.

Calculations of the frontier molecular orbitals for BTIC-1, BTIC-1′, and BTIC-2, together with their respective HOMO/LUMO energy levels are shown in in Figure 2a. The HOMO/LUMO were estimated to be −5.70/−3.47 eV for BTIC-1, −5.68/−3.43 eV for BTIC-1′ and −5.45/−3.51 eV for BTIC-2. To further investigate the differing molecular conformation on the absorption profile, time-dependent density functional theory (TD-DFT) was employed to calculate the first 30 excited states.[63,64] The wavelength, oscillator strength and molecular orbital (MO) contribution for each electronic transition are summarized in Table S1 (Supporting Information). As shown in Figure 2d, the calculated absorption of BTIC-2 is dominated by the $S_0 \rightarrow S_1$ transition (700.46 nm) that is red-shifted by 84.2 nm compared to the maximum absorption peak of BTIC-1 (616.26 nm), which is in line with the experimental trend shown in solution absorption spectra. (Figure 1a).

2.4. Organic Photodetectors

To investigate the photodetector properties of these two fully non-fused NFAs, BTIC-1 and BTIC-2 were blended with the polymer donor PM6 to fabricate OPDs with a device structure of indium tin oxide (ITO)/zinc oxide (ZnO)/PM6:BTIC/MoO_3/Ag (**Figure 3**a). The polymer PM6 was selected as the donor to afford a broadband OPD owing to the complementary absorption and well-matched energy levels with both acceptor materials (Figure S31, Supporting Information).[65] Devices were carefully optimized by tuning the solution concentrations, donor/acceptor ratios, spin-coating speeds and thermal annealing temperatures. As displayed in Figure 3b, the current density-voltage (*J-V*) characteristics of the OPDs were measured under AM 1.5G illumination (100 mW cm^{-2}) and in the dark. The OPDs comprising PM6:BTIC-2 exhibit a J_D value of 2.4×10^{-7} A cm^{-2} at -2 V, which is more than one order of magnitude lower compared to the J_D obtained by PM6:BTIC-1 devices (6.0×10^{-6} A cm^{-2}) at -2 V. Similarly, the current densities under light conditions were higher for BTIC-2-based devices (1.42×10^{-2} A cm^{-2}) compared to BTIC-1 (4.42×10^{-3} A cm^{-2}). Due to the instability under reverse bias and the low light-to-current conversion of PM6:BTIC-1, we therefore focused on the further optimization of PM6:BTIC-2 OPDs.

To quantify the spectral response of the OPDs depending on the incoming photons of certain energy, *R* of OPD devices was measured as a function of the incident light wavelength. Generally, *R* can be estimated from the Equation (3)

$$R = EQE \times q\lambda/hc \quad (3)$$

in which *h* is the Planck constant (6.626×10^{-34} J Hz^{-1}), λ is the wavelength of light and *c* is the speed of light (3.0×10^{8} m s^{-1}).[1,3] As depicted in Figure S32a (Supporting Information), *R* was measured at 0, −1 and -2 V. Figure 3c showed *R* of PM6:BTIC-2-based device, which exhibited a peak value of 0.36 A W^{-1} at 830 nm at a bias voltage of -2 V, which is comparable to commercially

© 2023 The Authors. Advanced Optical Materials published by Wiley-VCH GmbH

21951071, 2024, 6, Downloaded from https://onlinelibrary.wiley.com/doi/10.1002/adom.202302210 by Test, Wiley Online Library on [08/04/2024]. See the Terms and Conditions (https://onlinelibrary.wiley.com/terms-and-conditions) on Wiley Online Library for rules of use; OA articles are governed by the applicable Creative Commons License

available solid-state photodetectors.[66,67] We note that performing the characterization at a large reverse bias is important to correctly evaluate the figures of merit (see further discussion in Supporting Information).[68–70] D^* is another fundamental parameter of photodetectors and is usually employed to assess the light-detecting sensitivity (Figure 3c), which can be given by the Equation (4)

$$D^* = \frac{R\sqrt{A\Delta f}}{i_n} \tag{4}$$

where A denotes the photoactive area, Δf is the detection bandwidth and i_n is the noise current.[3,23] To accurately evaluate D^*, i_n was calculated by the fast Fourier transform of the current under an applied bias of -2 V. As shown in Figure S32b (Supporting Information), the OPDs based on the blend of PM6:BTIC-2 presented a i_n of 4.4×10^{-13} A, which is one order of magnitude higher than the value calculated from shot and thermal contributions. Owing to their low noise current, the OPDs based on PM6:BTIC-2 yielded a D^* value of 1.7×10^{11} Jones at 830 nm under the bias of -2 V. As depicted in Figure S32c (Supporting Information), D^* can be overestimated if i_n is calculated according to the Equation (5)

$$i_n = \sqrt{2qi_D + \frac{4kT}{R_{shunt}}} \tag{5}$$

where q is the elementary charge, k is Boltzmann constant, T is the temperature and R_{shunt} is derived from the respective J-V characteristics.[5,23]

Figure 3d and Figure S32d (Supporting Information) depict the dependence of response linearity on the modulated power of the white light source. The linear dynamic range (LDR) can be calculated by the Equation (6)

$$\mathrm{LDR} = 20\log\left(\frac{J_{\max}(V)}{J_{\min}(V)}\right) \tag{6}$$

where $J_{\max}$ and $J_{\min}$ are the photocurrent of the upper and lower limit of the linear range, respectively.[3,22] As a result, the LDR is calculated to be 72 dB. To evaluate the photo response speed of the OPDs, the response to temporal square-wave signal of PM6:BTIC-2-based OPDs under white light at -2 V and 2 kHz was studied (Figure 3e). The rise and fall times are defined as the time interval in which the current increases from 10% to 90% and transition from 90% down to 10% of the peak current, and were estimated to be 2.6 and 3.3 µs in our case, respectively. As a result, the response width at -3 dB point frequency (f_{-3dB}) of PM6:BTIC-2 reached 130 kHz, as shown in Figure 3f, which meets the requirement of real-time monitoring.[25,29]

Fabrication of OPDs using non-fused small-molecule acceptors has rarely been reported. Herein, the fully non-fused molecules BTIC demonstrate a more simplified chemical structure compared to other reported works which exhibit at least one fused component,[18,71] but exhibit comparable device performance with a responsivity of 0.36 A W^{-1} and detectivity of 1.7×10^{11} Jones at 830 nm. And the device using PM6:BTIC-2 delivered an ultrafast photo response with a lower rise time of 2.6 µs and a broader f_{-3dB} of 130 kHz.

2.5. Morphology Investigation

Grazing incidence wide-angle X-ray scattering (GIWAXS) was employed to investigate the molecular stacking and orientation of neat and blend films, prepared under the same conditions as those for the OPD devices (**Figure 4**a,b). All of them show a similar "edge-on" orientation as evidenced by the appearance of a lamellar (100) diffraction peak in the out-of-plane (OOP) direction and a π-π stacking (010) diffraction peak in the in-plane (IP) direction. The (100) peak was observed at $q = 3.22$ and 3.44 nm^{-1} for BTIC-1 and BTIC-2 respectively, with BTIC-2 exhibiting a more intense peak for films of comparable thickness. According to the Equation (7),[72]

$$d = 2\pi/q \tag{7}$$

the lamellar d-spacing distance of pristine BTIC-1 ad BTIC-2 were calculated to be 1.95 and 1.82 nm. The crystallite coherence lengths (CCLs) were calculated to be 17.1 nm for BTIC-1 and 17.6 nm for BTIC-2, based on Scherrer Equation (8).[73]

$$\tau = \frac{2\pi K}{FWHM} \tag{8}$$

These results indicate that BTIC-2 has a higher crystallinity and a more ordered molecular stacking than BTIC-1, which is consistent with modelling and UV–vis results. Both blend films of PM6:BTIC-1 and PM6:BTIC-2 show broader diffraction peaks compared to the corresponding neat films, indicating that in both cases blending reduced the crystallinity compared to pristine BTIC.

Atomic force microscopy (AFM) was further employed to investigate the influence of the backbone conformation on the surface morphology of the pristine BTIC and the blend of PM6:BTIC in the active layer for the fabricated devices. As shown in Figure 4c, both BTIC-1 and BTIC-2 exhibit fiber-shaped domains with a root mean square (RMS) of 2.79 nm for BTIC-1 and 12.37 nm for BTIC-2. The larger domain size and significantly increased roughness of pristine BTIC-2 film indicates stronger aggregation and nucleation relative to BTIC-1, which can be ascribed to the more favorable stacking behavior, due to the more planar backbone conformation of BTIC-2 as shown in Figure 2b, and the preference for a single conformer. Compared to pristine BTIC films, blending clearly reduces the crystallite size and surface roughness in both cases, which agrees well with GIWAXS results. There are no clear differences between the two blend films, but the reduced roughness in both cases suggests a good miscibility in the active layer, which is important for exciton harvesting and charge collection.[74,75]

3. Conclusion

In summary, two fully non-fused small-molecule acceptors (BTIC-1 and BTIC-2) were designed and employed for near-infrared organic photodetectors. Among them, BTIC-2 exhibits a

© 2023 The Authors. Advanced Optical Materials published by Wiley-VCH GmbH

21951071, 2024, 6, Downloaded from https://onlinelibrary.wiley.com/doi/10.1002/adom.202302210 by Test, Wiley Online Library on [08/04/2024]. See the Terms and Conditions (https://onlinelibrary.wiley.com/terms-and-conditions) on Wiley Online Library for rules of use; OA articles are governed by the applicable Creative Commons License

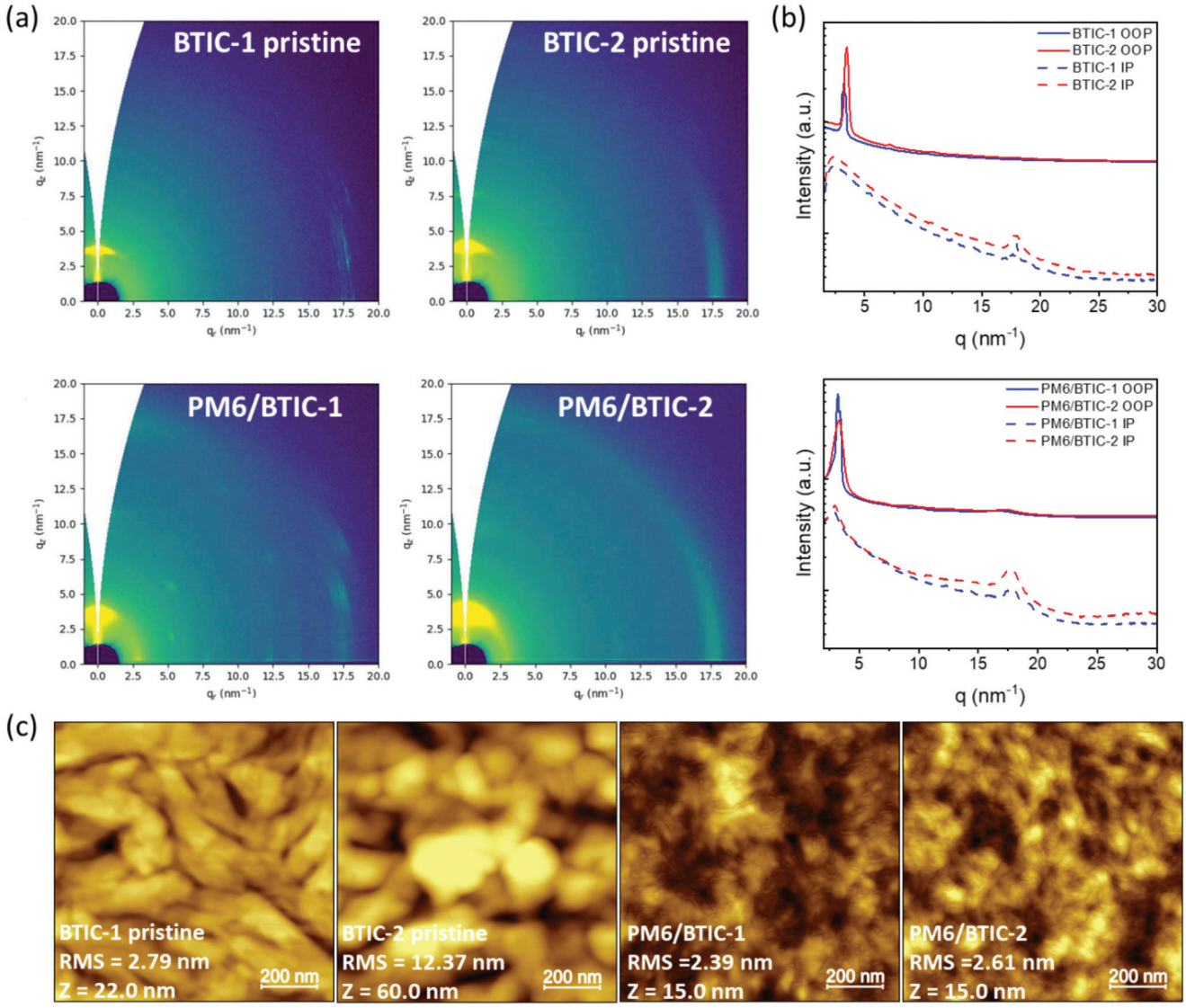


Figure 4. a) 2D GIWAXS images, b) corresponding in-plane and out-of-plane line cuts, c) AFM images of pristine BTIC and PM6:BTIC blends.

more coplanar structure and thus a more red-shifted absorption up to 900 nm, resulting from the increased conformational locks in BTIC-2 backbones. The relationship between the chemical structure of acceptor materials and the dark current was comprehensively explored by changing the position of the alkoxy side chain on the thiophene bridge. We found that by simply changing the position of side chain, a remarkable reduction of dark current (2.4×10^{-7} A cm^{-2}) was observed in the OPDs based on the blend of PM6:BTIC-2 with respect to that of PM6:BTIC-1, leading to a specific detectivity of 1.7×10^{11} Jones at 828 nm under the reverse bias of -2 V. An ultrafast response speed of 2.6 µs and a competent f_{-3dB} of 130 kHz were also achieved, suggesting the great promise of the present NIR OPDs herein. Theoretical calculation results and morphology studies indicate that the improved device performance can be ascribed to the more planar molecular backbone of BTIC-2 resulting from the increased non-covalent molecular conformational locks. Our work demonstrates that fully non-fused small molecules can play an important role in the practical application of NIR OPDs.

Supporting Information

Supporting Information is available from the Wiley Online Library or from the author.

Acknowledgements

X.H. and Z.Q. contributed equally to this work. The authors would like to thank the Engineering and Physics Science Research Council (EPSRC) (EP/V048686/1 and EP/T028513/1), the Royal Society and Wolfson Foundation, and the King Abdullah University of Science and Technology (KAUST) Office of Sponsored Research (OSR-2019-CRG8-4095) for financial support.

© 2023 The Authors. Advanced Optical Materials published by Wiley-VCH GmbH

21951071, 2024, 6, Downloaded from https://onlinelibrary.wiley.com/doi/10.1002/adom.202302210 by Test, Wiley Online Library on [08/04/2024]. See the Terms and Conditions (https://onlinelibrary.wiley.com/terms-and-conditions) on Wiley Online Library for rules of use; OA articles are governed by the applicable Creative Commons License

Conflict of Interest

The authors declare no conflict of interest.

Data Availability Statement

The data that support the findings of this study are available from the corresponding author upon reasonable request.

Keywords

acceptor, fully non-fused, intramolecular conformational interaction, near-infrared, organic photodetectors, small molecule

Received: September 11, 2023
Published online: October 12, 2023

[1] J. H. Kim, T. Schembri, D. Bialas, M. Stolte, F. Würthner, *Adv. Mater.* **2022**, *34*, 2104678.
[2] J. Han, F. Wang, S. Han, W. Deng, X. Du, H. Yu, J. Gou, Q. J. Wang, J. Wang, *Adv. Funct. Mater.* **2022**, *32*, 2205150.
[3] Y. Wang, J. Kublitski, S. Xing, F. Dollinger, D. Spoltore, J. Benduhn, K. Leo, *Mater. Horiz.* **2022**, *9*, 220.
[4] H. Anabestani, S. Nabavi, S. Bhadra, *Nanomaterials* **2022**, *12*, 3775.
[5] Z. Zhao, C. Xu, L. Niu, X. Zhang, F. Zhang, *Laser Photonics Rev.* **2020**, *14*, 2000262.
[6] P. C. Y. Chow, T. Someya, *Adv. Mater.* **2020**, *32*, 1902045.
[7] H. Anabestani, S. Nabavi, S. Bhadra, *Nanomaterials* **2022**, *12*, 3775.
[8] H. Ren, J.-D. Chen, Y.-Q. Li, J.-X. Tang, *Adv. Sci.* **2021**, *8*, 2002418.
[9] M.-K. Zhang, W.-D. Liu, Y.-P. Gong, Q. Liu, Z.-G. Chen, *Adv. Opt. Mater.* **2022**, *10*, 2201889.
[10] R. Guo, M. Zhang, J. Ding, A. Liu, F. Huang, M. Sheng, *J. Mater. Chem. C* **2022**, *10*, 7404.
[11] H.-Y. Hou, S. Tian, H.-R. Ge, J.-D. Chen, Y.-Q. Li, J.-X. Tang, *Adv. Funct. Mater.* **2022**, *32*, 2209324.
[12] Y. Zhang, Y. Ma, Y. Wang, X. Zhang, C. Zuo, L. Shen, L. Ding, *Adv. Mater.* **2021**, *33*, 2006691.
[13] Q. Qiu, Z. Huang, *Adv. Mater.* **2021**, *33*, 2008126.
[14] J. Zha, M. Luo, M. Ye, T. Ahmed, X. Yu, D.-H. Lien, Q. He, D. Lei, J. C. Ho, J. Bullock, K. B. Crozier, C. Tan, *Adv. Funct. Mater.* **2022**, *32*, 2111970.
[15] N. Li, P. Mahalingavelar, J. H. Vella, D.-S. Leem, J. D. Azoulay, T. N. Ng, *Mater. Sci. Eng. R: Rep.* **2021**, *146*, 100643.
[16] Y. Xu, Q. Lin, *Appl. Phys. Rev.* **2020**, *7*, 011315.
[17] C. Xie, C.-K. Liu, H.-L. Loi, F. Yan, *Adv. Funct. Mater.* **2020**, *30*, 1903907.
[18] S. Deng, L. Zhang, J. Zheng, J. Li, S. Lei, Z. Wu, D. Yang, D. Ma, J. Chen, *Adv. Opt. Mater.* **2022**, *10*, 2200371.
[19] C. Labanti, J. Wu, J. Shin, S. Limbu, S. Yun, F. Fang, S. Y. Park, C.-J. Heo, Y. Lim, T. Choi, H.-J. Kim, H. Hong, B. Choi, K.-B. Park, J. R. Durrant, J.-S. Kim, *Nat. Commun.* **2022**, *13*, 3745.
[20] D. Zhu, D. Ji, L. Li, W. Hu, *J. Mater. Chem. C* **2022**, *10*, 13312.
[21] K. Kudo, T. Moriizumi, *Appl. Phys. Lett.* **1981**, *39*, 609.
[22] W. Xu, Y. Gao, K. Qian, B. Wang, R. Xu, M. He, T. Li, G. Xing, S. Yang, G. Wei, *J. Mater. Chem. C* **2022**, *10*, 9391.
[23] T. Zhang, M. Moser, A. D. Scaccabarozzi, H. Bristow, P. Jacoutot, A. Wadsworth, T. D. Anthopoulos, I. McCulloch, N. Gasparini, *J. Phys.: Mater.* **2021**, *4*, 045001.
[24] N. Gasparini, A. Gregori, M. Salvador, M. Biele, A. Wadsworth, S. Tedde, D. Baran, I. Mcculloch, C. J. Brabec, *Adv. Mater. Technol.* **2018**, *3*, 1800104.
[25] X. Liao, W. Xie, Z. Han, Y. Cui, X. Xia, X. Shi, Z. Yao, X. Xu, X. Lu, Y. Chen, *Adv. Funct. Mater.* **2022**, *32*, 2204255.
[26] J. Huang, J. Lee, J. Vollbrecht, V. V. Brus, A. L. Dixon, D. X. Cao, Z. Zhu, Z. Du, H. Wang, K. Cho, G. C. Bazan, T.-Q. Nguyen, *Adv. Mater.* **2020**, *32*, 1906027.
[27] Y. Song, G. Yu, B. Xie, K. Zhang, F. Huang, *Appl. Phys. Lett.* **2020**, *117*, 093302.
[28] Y. Zhang, Q. Wei, Z. He, Y. Wang, T. Shan, Y. Fu, X. Guo, H. Zhong, *ACS Appl. Mater. Interfaces* **2022**, *14*, 31066.
[29] J. H. Kim, A. Liess, M. Stolte, A.-M. Krause, V. Stepanenko, C. Zhong, D. Bialas, F. Spano, F. Würthner, *Adv. Mater.* **2021**, *33*, 2100582.
[30] Y. Chen, Y. Zheng, Y. Jiang, H. Fan, X. Zhu, *J. Am. Chem. Soc.* **2021**, *143*, 4281.
[31] P. Jacoutot, A. D. Scaccabarozzi, T. Zhang, Z. Qiao, F. Aniés, M. Neophytou, H. Bristow, R. Kumar, M. Moser, A. D. Nega, A. Schiza, A. Dimitrakopoulou-Strauss, V. G. Gregoriou, T. D. Anthopoulos, M. Heeney, I. Mcculloch, A. A. Bakulin, C. L. Chochos, N. Gasparini, *Small* **2022**, *18*, 2200580.
[32] J. Vanderspikken, Q. Liu, Z. Liu, T. Vandermeeren, T. Cardeynaels, S. Gielen, B. Van Mele, N. Van Den Brande, B. Champagne, K. Vandewal, W. Maes, *Adv. Funct. Mater.* **2022**, *32*, 2108146.
[33] J. H. Vella, L. Huang, N. Eedugurala, K. S. Mayer, T. N. Ng, J. D. Azoulay, *Sci. Adv.* **2021**, *7*, eabg2418.
[34] Z. Wu, Y. Zhai, H. Kim, J. D. Azoulay, T. N. Ng, *Acc. Chem. Res.* **2018**, *51*, 3144.
[35] R. D. Jansen-Van Vuuren, A. Armin, A. K. Pandey, P. L. Burn, P. Meredith, *Adv. Mater.* **2016**, *28*, 4766.
[36] S. Gielen, C. Kaiser, F. Verstraeten, J. Kublitski, J. Benduhn, D. Spoltore, P. Verstappen, W. Maes, P. Meredith, A. Armin, K. Vandewal, *Adv. Mater.* **2020**, *32*, 2003818.
[37] B. Xie, R. Xie, K. Zhang, Q. Yin, Z. Hu, G. Yu, F. Huang, Y. Cao, *Nat. Commun.* **2020**, *11*, 2871.
[38] C. Wang, X. Zhang, W. Hu, *Chem. Soc. Rev.* **2020**, *49*, 653.
[39] J. Miao, F. Zhang, Y. Lin, W. Wang, M. Gao, L. Li, J. Zhang, X. Zhan, *Adv. Opt. Mater.* **2016**, *4*, 1711.
[40] G. Simone, M. J. Dyson, C. H. L. Weijtens, S. C. J. Meskers, R. Coehoorn, R. A. J. Janssen, G. H. Gelinck, *Adv. Opt. Mater.* **2020**, *8*, 1901568.
[41] P. E. Keivanidis, P. K. H. Ho, R. H. Friend, N. C. Greenham, *Adv. Funct. Mater.* **2010**, *20*, 3895.
[42] W. Yang, W. Qiu, E. Georgitzikis, E. Simoen, J. Serron, J. Lee, I. Lieberman, D. Cheyns, P. Malinowski, J. Genoe, H. Chen, P. Heremans, *ACS Appl. Mater. Interfaces* **2021**, *13*, 16766.
[43] Z. Zhong, F. Peng, Z. Huang, L. Ying, G. Yu, F. Huang, Y. Cao, *ACS Appl. Mater. Interfaces* **2020**, *12*, 45092.
[44] O. J. Sandberg, C. Kaiser, S. Zeiske, N. Zarrabi, S. Gielen, W. Maes, K. Vandewal, P. Meredith, A. Armin, *Nat. Photonics* **2023**, *17*, 368.
[45] L. Zhang, T. Yang, L. Shen, Y. Fang, L. Dang, N. Zhou, X. Guo, Z. Hong, Y. Yang, H. Wu, J. Huang, Y. Liang, *Adv. Mater.* **2015**, *27*, 6496.
[46] J. Kublitski, A. Hofacker, B. K. Boroujeni, J. Benduhn, V. C. Nikolis, C. Kaiser, D. Spoltore, H. Kleemann, A. Fischer, F. Ellinger, K. Vandewal, K. Leo, *Nat. Commun.* **2021**, *12*, 551.
[47] A. Armin, W. Li, O. J. Sandberg, Z. Xiao, L. Ding, J. Nelson, D. Neher, K. Vandewal, S. Shoaee, T. Wang, H. Ade, T. Heumüller, C. Brabec, P. Meredith, *Adv. Energy Mater.* **2021**, *11*, 2003570.
[48] T.-J. Wen, D. Wang, L. Tao, Y. Xiao, Y.-D. Tao, Y. Li, X. Lu, Y. Fang, C.-Z. Li, H. Chen, D. Yang, *ACS Appl. Mater. Interfaces* **2020**, *12*, 39515.
[49] Q. Shen, C. He, S. Li, L. Zuo, M. Shi, H. Chen, *Acc. Mater. Res.* **2022**, *3*, 644.
[50] M. Yang, W. Wei, X. Zhou, Z. Wang, C. Duan, *Energy Mater.* **2021**, *1*, 100008.
[51] L. Lv, J. Yu, X. Sui, J. Wu, X. Dong, G. Lu, X. Liu, A. Peng, H. Huang, *J. Mater. Chem. C* **2019**, *7*, 5739.

© 2023 The Authors. Advanced Optical Materials published by Wiley-VCH GmbH

21951071, 2024, 6, Downloaded from https://onlinelibrary.wiley.com/doi/10.1002/adom.202302210 by Test, Wiley Online Library on [08/04/2024]. See the Terms and Conditions (https://onlinelibrary.wiley.com/terms-and-conditions) on Wiley Online Library for rules of use; OA articles are governed by the applicable Creative Commons License

[52] Q. He, M. Shahid, X. Jiao, E. Gann, F. D. Eisner, T. Wu, Z. Fei, T. D. Anthopoulos, C. R. McNeill, M. Heeney, *ACS Appl. Mater. Interfaces* **2020**, *12*, 9555.
[53] T. J. Aldrich, M. Matta, W. Zhu, S. M. Swick, C. L. Stern, G. C. Schatz, A. Facchetti, F. S. Melkonyan, T. J. Marks, *J. Am. Chem. Soc.* **2019**, *141*, 3274.
[54] W. Zhao, S. Li, H. Yao, S. Zhang, Y. Zhang, B. Yang, J. Hou, *J. Am. Chem. Soc.* **2017**, *139*, 7148.
[55] Z.-P. Yu, Z.-X. Liu, F.-X. Chen, R. Qin, T.-K. Lau, J.-L. Yin, X. Kong, X. Lu, M. Shi, C.-Z. Li, H. Chen, *Nat. Commun.* **2019**, *10*, 2152.
[56] Z.-X. Liu, Z.-P. Yu, Z. Shen, C. He, T.-K. Lau, Z. Chen, H. Zhu, X. Lu, Z. Xie, H. Chen, C.-Z. Li, *Nat. Commun.* **2021**, *12*, 3049.
[57] Z. Fei, X. Gao, J. Smith, P. Pattanasattayavong, E. Buchaca Domingo, N. Stingelin, S. E. Watkins, T. D. Anthopoulos, R. J. Kline, M. Heeney, *Chem. Mater.* **2013**, *25*, 59.
[58] H. Usta, D. Alimli, R. Ozdemir, E. Tekin, F. Alkan, R. Kacar, A. G. Altas, S. Dabak, A. G. Gürek, E. Mutlugun, A. F. Yazici, A. Can, *J. Mater. Chem. C* **2020**, *8*, 8047.
[59] W. Gao, H. Fu, Y. Li, F. Lin, R. Sun, Z. Wu, X. Wu, C. Zhong, J. Min, J. Luo, H. Y. Woo, Z. Zhu, A. K.-Y. Jen, *Adv. Energy Mater.* **2021**, *11*, 2003177.
[60] A. Shafiee, M. Mat Salleh, M. Yahaya, *Sains Malays.* **2011**, *40*, 173.
[61] Q. He, M. Shahid, J. Panidi, A. V. Marsh, W. Huang, M. Daboczi, J.-S. Kim, Z. Fei, T. D. Anthopoulos, M. Heeney, *J. Mater. Chem. C* **2019**, *7*, 6622.
[62] A. Creamer, A. Casey, A. V. Marsh, M. Shahid, M. Gao, M. Heeney, *Macromolecules* **2017**, *50*, 2736.
[63] Y. Cui, P. Zhu, X. Liao, Y. Chen, *J. Mater. Chem. C* **2020**, *8*, 15920.
[64] Q. He, F. D. Eisner, D. Pearce, T. Hodsden, E. Rezasoltani, D. Medranda, Z. Fei, J. Nelson, M. Heeney, *J. Mater. Chem. C* **2020**, *8*, 17237.
[65] M. Zhang, X. Guo, W. Ma, H. Ade, J. Hou, *Adv. Mater.* **2015**, *27*, 4655.
[66] M. Biele, C. Montenegro Benavides, J. Hürdler, S. F. Tedde, C. J. Brabec, O. Schmidt, *Adv. Mater. Technol.* **2019**, *4*, 1800158.
[67] H. Xu, J. Liu, J. Zhang, G. Zhou, N. Luo, N. Zhao, *Adv. Mater.* **2017**, *29*, 1700975.
[68] T. Kamijo, A. J. J. M. Van Breemen, X. Ma, S. Shanmugam, T. Bel, G. De Haas, B. Peeters, R. Petre, D. Tordera, R. Verbeek, H. B. Akkerman, L. M. Hagelsieb, F. De Roose, I. Lieberman, F. Yamaguchi, R. A. J. Janssen, E. A. Meulenkamp, A. J. Kronemeijer, G. H. Gelinck, *Nat. Electron.* **2023**, *6*, 451.
[69] X. Ma, H. Bin, B. T. Van Gorkom, T. P. A. Van Der Pol, M. J. Dyson, C. H. L. Weijtens, M. Fattori, S. C. J. Meskers, A. J. J. M. Van Breemen, D. Tordera, R. A. J. Janssen, G. H. Gelinck, *Adv. Mater.* **2023**, *35*, 2209598.
[70] P. Jacoutot, A. D. Scaccabarozzi, D. Nodari, J. Panidi, Z. Qiao, A. Schiza, A. D. Nega, A. Dimitrakopoulou-Strauss, V. G. Gregoriou, M. Heeney, C. L. Chochos, A. A. Bakulin, N. Gasparini, *Sci. Adv.* **2023**, *9*, eadh2694.
[71] M. S. Kim, D. Luo, W. Jang, B. G. Kim, C. Shan, A. K. K. Kyaw, D. H. Wang, *Adv. Opt. Mater.* **2023**, *11*, 2202525.
[72] X. Tao, W. Li, Q. Wu, H. Wei, Y. Yan, L. Zhao, Y. Hu, Y. Zhao, H. Chen, Y. Liu, *Adv. Funct. Mater.* **2023**, *33*, 2210846.
[73] A. Mahmood, J.-L. Wang, *Sol. RRL* **2020**, *4*, 2000337.
[74] J. Wu, Y. Xu, Z. Yang, Y. Chen, X. Sui, L. Yang, P. Ye, T. Zhu, X. Wu, X. Liu, H. Cao, A. Peng, H. Huang, *Adv. Energy Mater.* **2019**, *9*, 1803012.
[75] J. Chang, Y. Kuga, I. Mora-Seró, T. Toyoda, Y. Ogomi, S. Hayase, J. Bisquert, Q. Shen, *Nanoscale* **2015**, *7*, 5446.

© 2023 The Authors. Advanced Optical Materials published by Wiley-VCH GmbH

21951071, 2024, 6, Downloaded from https://onlinelibrary.wiley.com/doi/10.1002/adom.202302210 by Test, Wiley Online Library on [08/04/2024]. See the Terms and Conditions (https://onlinelibrary.wiley.com/terms-and-conditions) on Wiley Online Library for rules of use; OA articles are governed by the applicable Creative Commons License